View Article Online
View Journal

Journal of Materials Chemistry A

Materials for energy and sustainability

Accepted Manuscript

This article can be cited before page numbers have been issued, to do this please use: U. N. Pan, T. I. Singh, D. R. Paudel, C. C. GUDAL, N. H. Kim and J. H. Lee, *J. Mater. Chem. A*, 2020, DOI: 10.1039/D0TA05865C.

ROYAL SOCIETY OF CHEMISTRY

rsc.li/materials-a

View Article Online
DOI: 10.1039/D0TA05865C

ARTICLE

Received 00th January 20xx,

Accepted 00th January 20xx

DOI: 10.1039/x0xx00000x

Covalent–doping of Ni and P for 1T–enriched MoS_2 bifunctional 2D–nanostructures with active basal planes and expanded interlayers boosting electrocatalytic water splitting

Uday Narayan Pan[a], Thangjam Ibomcha Singh[a], Dasu Ram Paudel[a], Chandan Chandru Gudal[a], Nam Hoon Kim[a]*, Joong Hee Lee[a,b]*

Electrocatalytic water-splitting performance of MoS_2 nanostructures can be improved by increasing edge density, activating basal planes, expanding interlayer spacing and stabilizing the 1T-phase. In this work, for the first time, we have studied the synchronous involvement of all these driving factors to achieve the highest bifunctional performance of MoS_2 for water-splitting following doping and intercalation of nickel (Ni) and phosphorus (P) in a single-step reaction. Two nanostructures, nanoflowers (1T-$Ni_{0.2}Mo_{0.8}S_{1.8}P_{0.2}$ NFs, powder) for large scale synthesis and freestanding nanosheet on carbon-cloth (1T-$Ni_{0.2}Mo_{0.8}S_{1.8}P_{0.2}$ NS/CC) as binder-free electrode are fabricated. Co-doping of Ni and P enriches the 1T-phase, expands interlayer spacing by 24%, activates basal planes significantly and increase the edge density of MoS_2 in the 2D-nanostructures. The 1T-$Ni_{0.2}Mo_{0.8}S_{1.8}P_{0.2}$ NS/CC and 1T-$Ni_{0.2}Mo_{0.8}S_{1.8}P_{0.2}$ NFs exhibit significantly low overpotentials of 55 and 99 mV at the current density of 10 mA cm^{-2} for the hydrogen evolution reaction (HER) and 286 and 305 mV at 40 mA cm^{-2} for the oxygen evolution reaction (OER), respectively. Further, 1T-$Ni_{0.2}Mo_{0.8}S_{1.8}P_{0.2}$-NS/CC (+ -) and 1T-$Ni_{0.2}Mo_{0.8}S_{1.8}P_{0.2}$-NFs (+ -) alkaline electrolyzers require only 1.52 and 1.53 V, respectively, to generate a current density of 20 mA cm^{-2} with robust stability, much superior to recently reported electrocatalysts, indicating the immense potential of the employed strategy for developing highly efficient and low-cost electrocatalyst for water-splitting.

Introduction

Electrocatalytic water-splitting is considered as the best method for converting energy obtained from renewable resources into clean hydrogen fuel (H_2-fuel).[1–5] Large scale storage of energy as H_2-fuel will reduce the requirements of fossil fuels and that will eventually lead to massive reduction in environmental pollution.[1–5] The electrocatalytic water-splitting is fundamentally a combination of two half-reactions, hydrogen evolution reaction (HER) and oxygen evolution reaction (OER). Iridium (Ir), ruthenium (Ru) and their oxides are major commercially offered OER catalysts whereas, platinum (Pt) is considered as the best HER catalyst. However, their tiny abundancy in the Earth's crust has created major obstacles in the large-scale utilization of this technique.[1–5] In search of alternative catalyst for scaling up the process, metal chalcogenides were proposed as the possible alternatives due to their huge availability and low cost.[3,6–9] Among different metal chalcogenides, di-sulfide of molybdenum (MoS_2), is not only very cheap and highly abundant, but has lowest propensity for causing environmental and health hazards. Thus, it was considered as an ideal alternative for replacing the commercially available but highly expensive electrocatalysts.[3,7–12] Furthermore, its layered structure like graphite, high conductivity, ease of synthesis, and robust electrochemical, mechanical and chemical durability made MoS_2 more attractive and lucrative alternative compared to other transition metal chalcogenides.[3,7,8,10,11] MoS_2 also possesses unique crystallographic phases like 2H (D_{3h}, semiconducting) and 1T (O_h, metallic) with unique electronic characteristics, which can be tuned for activating the basal planes and increasing the conductivity.[13–17]

Bulk MoS_2 crystal was found to be inactive for electrocatalytic water splitting back in 1970s.[3,12] However, progressive research has established that (1010) molybdenum-edges (Mo-edges) of the MoS_2 nanostructures do participate in the HER catalysis, and their computational free energy of hydrogen bonding is near to that of the Pt-catalyst.[3,12,18,19] This has opened up significant opportunities for exploring the HER catalysis of MoS_2 by manipulating the edge structures and density. Subsequently, nanostructures with very fine and high edge-density were produced to increase the active catalytic sites, which has achieved significant success.[3,8,12] For further

[a.] Advanced Materials Institute of BIN Convergence Technology (BK21 plus Global) and Department of BIN Convergence Technology, Jeonbuk National University, Jeonju, Jeonbuk, 54896, Republic of Korea.
[b.] Carbon Composite Research Centre, Department of Polymer-Nano Science and Technology, Jeonbuk National University, Jeonju, Jeonbuk 54896, Republic of Korea.

†Electronic Supplementary Information (ESI) available: [FESEM images and BET study of control materials, CV plots for ECSA calculation, EIS plots, LSV based stability test and comparison table]. See DOI: 10.1039/x0xx00000x

E-mail: jhl@jbnu.ac.kr (Joong Hee Lee), nhk@jbnu.ac.kr (Nam Hoon Kim)

View Article Online
DOI: 10.1039/D0TA05865C

boosting the HER performances of MoS_2, recently, other important parameters such as activation of the latent basal planes, reduction in band gap and expansion in interlayer distances have also been taken into account.[8,10,12] In this regard, doping of the transition metals has found to alter the core electronic structure of the pristine MoS_2 by manipulating the electron density around Mo, which significantly reduces the hydrogen adsorption free energy.[7,20–22] In contrast, non-metal doping like phosphorus (P) has been found to activate the basal planes and expand the interlayer distances greatly.[7,10,23–25] Active basal planes produce an enormously large number of able sites for catalysis, that otherwise remain sluggish even in very fine nanostructures of MoS_2.[7,10,23–25] On the other hand, expansion in the interlayer spacing too rises the number of catalytically active sites by allowing directional passage of the electrolyte to the very core of the material and triggers smooth hydrogen adsorption and release simulteniously.[7,10,23–25] Another important factor that greatly influence electrocatalytic efficiency of a material is its intrinsic conductivity.[7,26] Although the transition-metal chalcogenides have higher intrinsic conductivity than do their oxide or hydroxide counterpart, but that is nowhere similar to the carbon based 2D materials like graphene.[7,21,27–29] To circumvent the issue, simple modification in the core structure of MoS_2 was proposed to play a very effective role in boosting its intrinsic conductivity even up to the metallic level.[13–15,31–33] The 2D-structure of MoS_2, consists of one molybdenum atom (Mo) surrounded by two sulfur (S) atoms to produce S-Mo-S triatomic planes.[13–15,31–33] The dissimilar possibility in the arrangement of the S-atoms leads to the occurrence of polymorphism with two crystallographic phases having different electronic structures, semiconducting D_{3h}-trigonal prismatic 2H-phase, and metallic O_h-octahedral 1T-phase. The semiconducting 2H-phase, is thermodynamically more stable, but it has lower conductivity and inactive basal planes for catalytic water-splitting, whereas, the metastable 1T-phase has very high conductivity like metal as well as active basal planes; hence, it is more potent as a catalyst.[13–15,31–33] The only but effective way to overcome the metastability challenge of 1T-MoS_2 is intercalation of transition metals or alkali metals as electron donors to the host.[13–15,31–33] Apart from stabilizing the 1-T phase, transition metals also activate unsaturated Mo and S sites; thus, alkali metals were ignored, and prominent transition-metal nickel (Ni) intercalation is considered in the present study. Primarily, Ni has a very high affinity towards S and forms a strong Ni-S bond, in both the hexagonal (alpha) and rhombohedral (beta) unit cells, and can also acts as an electron donor to the host phase; thus, it has the potential to stabilize the 1T-phase of MoS_2 with an enormously high number of active basal planes for water splitting.[13–15,31–33] The high conductivity of 1T-MoS_2 also facilitates fast charge-transport kinetics in the electrode-electrolyte interface, which also holds a high potential for significantly improving the catalytic efficacy.[13–15,31–33] Still, the driving factors namely, activation of basal planes, increase in interlayer spacing, and enrichment of the 1T-phase were studied distinctly for improving the catalytic efficacy of MoS_2 nanostructures by either transition metal or non-metal doping. However, the outcome of their synchronized effect has not been studied so far.[7,10,23–25,27] Although, to get best HER performance for MoS_2, the only way is to develop a single nanomaterial where all the possible driving factors are simultaneously active and yield an additive or synergistic performance. Taking this in account, for the first time to the best of our knowledge, we have focused on activating the basal planes, expansion of the interlayer spacing, and improving the conductivity following enrichment in the 1T-phase in a ultrathin nanosheet structure with active edges in tandem to get highest possible HER performance of MoS_2.

Now, since MoS_2 was found to have poor OER catalytic efficacy, most research regarding MoS_2 as a water-splitting catalyst was largely focused on improving its HER performance, and very little attention was paid on improving its OER catalytic efficiency.[3,8,12,34,35] But, from the viewpoint of large-scale industrial utility, fabrication of a bifunctional catalyst having strong HER and OER electrocatalytic efficacy in the same electrolyte is certainly the main goal for the best productivity at low cost.[7,21,36,37] Covalent doping of transition metals (TMs) on MoS_2 has been studied very recently as an effective approach for improving the catalytic OER efficiency in alkaline medium.[7,21,27–29] Doping of TMs alters the core electronic structure of the MoS_2 to enhance OER performances and generates additional sites.[7,21,27–29] In the present study, presence of Ni not only improves the catalytic HER performance, but also simultaneously generates OER active sites, introducing true bifunctionality to the material.[7,21,27–29] Moreover, Ni-doping also enhances the intrinsic OER performance of MoS_2 by altering the electron density around Mo.[7,21,27–29].

Herein, we have synthesized two different nanostructures of the P and Ni intercalated and doped 1T-MoS_2 in a single-step reaction. The free-standing nanosheets on carbon cloth (1T-$Ni_{0.2}Mo_{0.8}S_{1.8}P_{0.2}$ NS/CC) were fabricated as binder-free electrodes and the powder nanoflowers (1T-$Ni_{0.2}Mo_{0.8}S_{1.8}P_{0.2}$ NFs) for large-scale synthesis. Co-doping helps in the enrichment of 1T-phase of MoS_2 and as P-doped MoS_2 and 1T-MoS_2 both have active basal planes thus, doping of P on 1T-MoS_2 produces an enormously large number of active basal planes for water-splitting. 1T-$Ni_{0.2}Mo_{0.8}S_{1.8}P_{0.2}$ also has a significantly high concentration of functional ultrathin edges, together with active basal planes that generates synergistic improvements in the catalytic efficacy. Moreover, a significant increase in interlayer spacing (24%) is also observed; this allows smooth passage of the electrolyte and thus, facilitates the electrolyte to interact with more active centers. The presence of Ni also generates additional OER active sites in the host and in tandem boosts the inherent OER ability of MoS_2, leading to the formulation of a true bifunctional catalyst for water-splitting. 1T-$Ni_{0.2}Mo_{0.8}S_{1.8}P_{0.2}$, in the present study exhibited exceptional HER, OER and overall water-splitting performances with significantly high durability. Thus, the present materials and the approach could be apprehended as novel and together hold immense potential to significantly contribute to the current research regarding development of

View Article Online
DOI: 10.1039/D0TA05861C

highly efficient, low-cost electrocatalysts based on the earth abundant materials.

Experimental

Preparation of chemical mixture for the synthesis of the catalysts

The precursor salts, namely sodium molybdate dihydrate [$Na_2MoO_4.2H_2O$], nickel(II) acetate tetrahydrate [$Ni(OCOCH_3)_2{\cdot}4H_2O$], L-cysteine [$HSCH_2CH(NH_2)CO_2H$] and sodium phosphate monobasic [NaH_2PO_4] were mixed in 4 : 1 : 45 : 5 molar ratio using water as solvent. The mixture was then sonicated for 15 min and then vigorously mixed by magnetic stirring using a Teflon-coated magnetic bar for 1 h at room temperature. This mixture is termed here *mixture 1*.

Fabrication of 1T-$Ni_{0.2}Mo_{0.8}S_{1.8}P_{0.2}$ NFs

For the synthesis of 1T-$Ni_{0.2}Mo_{0.8}S_{1.8}P_{0.2}$ NFs mixture-1 was directly transferred to the Teflon-lined autoclave and incubated at 190 °C for 18 h. After completion of the reaction the powder was collected and washed with water-ethanol mixture for several times and then dried at 60°C temperature. Then an ink was prepared by mixing 3 mg of 1T-$Ni_{0.2}Mo_{0.8}S_{1.8}P_{0.2}$ NFs dried powder, 750 mL of isopropyl alcohol 50 mL of nafion–117 and 200 mL of DI water and sonicated for 30 min. This ink was then coated on a carbon cloth (CC, 1 cm^2 area) to prepare the electrode.

Fabrication of 1T-$Ni_{0.2}Mo_{0.8}S_{1.8}P_{0.2}$ NS/CC

For the fabrication of *1T-$Ni_{0.2}Mo_{0.8}S_{1.8}P_{0.2}$ NS/CC mixture-1* was transferred to the Teflon-lined autoclave then a clean carbon cloth (CC) was dipped into it. The reaction was carried out at the same condition i.e., 190 °C for 18 h. Once the reaction was finished, the carbon cloth was taken out and washed with water-ethanol mixture several times and finally, dried at 60°C. *1T-$Ni_{0.2}Mo_{0.8}S_{1.8}P_{0.2}$ NS* was found to grow on the carbon cloth and then the carbon cloth, which was then cut into 1 cm x 1 cm pieces and used as electrode for electrochemical analysis.

Synthesis of control materials:

Control materials were synthesized using the same reaction conditions. Briefly, for MoS_2 sodium molybdate dihydrate [$Na_2MoO_4.2H_2O$] and L-cysteine were mixed in 1:10 molar ratio, for Ni-MoS_2 sodium molybdate dihydrate [$Na_2MoO_4.2H_2O$], nickel(II) acetate tetrahydrate [$Ni(OCOCH_3)_2{\cdot}4H_2O$] and L-cysteine [$HSCH_2CH(NH_2)CO_2H$] were mixed in 4 : 1 : 50 molar ratio and for the synthesis of P-MoS_2 sodium molybdate dihydrate [$Na_2MoO_4.2H_2O$], L-cysteine [$HSCH_2CH(NH_2)CO_2H$] and sodium phosphate monobasic [NaH_2PO_4] were mixed in 1 : 9 : 1 ratio. Water was used as the solvent for synthesis of all the materials and the reaction was carried out in hydrothermal incubation at 190 °C for 18 h. All the powder samples were coated on carbon cloth using an ink preparation method similar to that of *1T-$Ni_{0.2}Mo_{0.8}S_{1.8}P_{0.2}$ NFs*.

Electrochemical characterizations

Electrochemical characterizations of all the samples was carried out in a CHI 660D electrochemical workstation (maker: CH Instruments Inc.,USA) using Ag/AgCl as the reference electrode and a graphite rod as the counter electrode. The 1T-$Ni_{0.2}Mo_{0.8}S_{1.8}P_{0.2}$ NFs coated carbon cloth and freestanding 1T-$Ni_{0.2}Mo_{0.8}S_{1.8}P_{0.2}$ NS/CC of size 1 cm^2 was used as the working electrode and N_2-saturated 1 (M) KOH was used as electrolyte for the electrochemical measurements. For comparison, RuO_2-C and Pt-C were coated on the carbon cloth surface (1cm^2) using the similar ink preparation method mentioned above and used as the working electrodes. The electrochemical active surface area (ECSA) is determined using following equation ECSA=C_{dl}/C_s, where C_s is the specific capacitance of flat surface and C_{dl} is the electrochemical double layer capacitance.[37,38]

Calculation of potential vs. RHE

All potentials were measured using Ag/AgCl as the reference electrode and later were converted to potential vs. RHE using the following equation *(1)* [37,38]

$E_{RHE} = E_{Ag/AgCl} + 0.059pH + E^{O}_{Ag/AgCl}$ .....*(1)*

iR corrected LSV plotting

iR corrected LSV was plotted using equation (2) [37,38]

$E_c = E_m - iR_s$.....(2)

where E_c is the iR corrected potential, E_m is the measured potential and R_s is the equivalent series resistance.

Results and discussion

Structural and Morphological Characterizations of 1T-$Ni_{0.2}Mo_{0.8}S_{1.8}P_{0.2}$ NFs and 1T-$Ni_{0.2}Mo_{0.8}S_{1.8}P_{0.2}$ NS/CC

Ni and P intercalated and doped 1T-enriched MoS_2 nanosheets on carbon cloth (CC) (1T-$Ni_{0.2}Mo_{0.8}S_{1.8}P_{0.2}$ NS/CC) and nanoflowers in powder form (1T-$Ni_{0.2}Mo_{0.8}S_{1.8}P_{0.2}$ NFs), were synthesized in a simple one-pot scalable hydrothermal

View Article Online
DOI: 10.1039/D0TA05865C

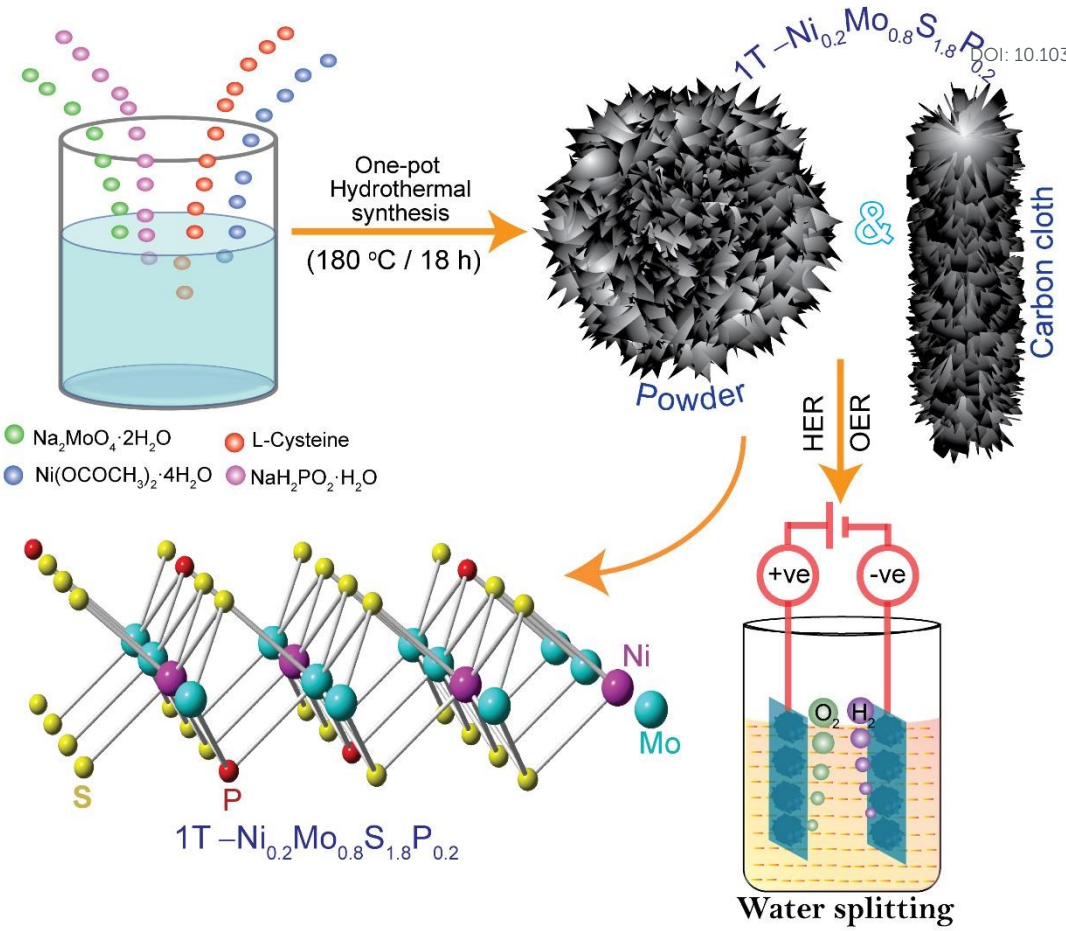

Scheme 1. Schematic representation of the fabrication of 1T-$Ni_{0.2}Mo_{0.8}S_{1.8}P_{0.2}$ NS/CC and 1T-$Ni_{0.2}Mo_{0.8}S_{1.8}P_{0.2}$ NFs and its application in overall electrochemical water splitting.

approach (as described in the experimental section, **Scheme 1**).[7,10,21,23] In one single reaction, up to 5 g of the 1T-$Ni_{0.2}Mo_{0.8}S_{1.8}P_{0.2}$ NFs was synthesized, and with proper setup the reaction could be scaled to much higher level to satisfy the demand of industry. Synthesis of MoS_2, P-doped MoS_2 (P-MoS_2) and Ni-doped MoS_2 (Ni-MoS_2) nanostructures were also carried out in a similar condition as control materials (details in experimental section). It was reported in many literatures that the ~20% of the transition metal and ~10% of nonmetal doping is ideal for optimal improvement of the HER and OER performance of MoS_2.[7,10,20,23,25,27,39] In the present study 20% Ni and 10% P doped and intercalated in the MoS_2 nanostructures were found to produce best catalytic efficacy compared to catalysts with other doping concentration of Ni and P, namely $Ni_{0.1}Mo_{0.9}S_{1.8}P_{0.2}$, $Ni_{0.3}Mo_{0.7}S_{1.8}P_{0.2}$, $Ni_{0.2}Mo_{0.8}S_{1.7}P_{0.3}$, $Ni_{0.2}Mo_{0.8}S_{1.9}P_{0.1}$, $Ni_{0.1}Mo_{0.9}S_{1.7}P_{0.3}$, $Ni_{0.1}Mo_{0.9}S_{1.9}P_{0.1}$, $Ni_{0.3}Mo_{0.7}S_{1.7}P_{0.3}$, $Ni_{0.3}Mo_{0.7}S_{1.9}P_{0.1}$. Moreover, a relatively low Ni contain will also eliminate the possibility of the formation of any undesired MoS_2-NiS side product.[39,40] The molar ratio of the precursor metal salts (Ni:Mo) was kept 1:4 and the molar ratio of the precursors nonmetals (S:P) was kept 9:1 prior to the reaction. The elemental composition of the materials was later verified using atomic absorption spectroscopy (AAS) and inductively coupled plasma-optical emission spectrometry (ICP-OES, **Table S1**).

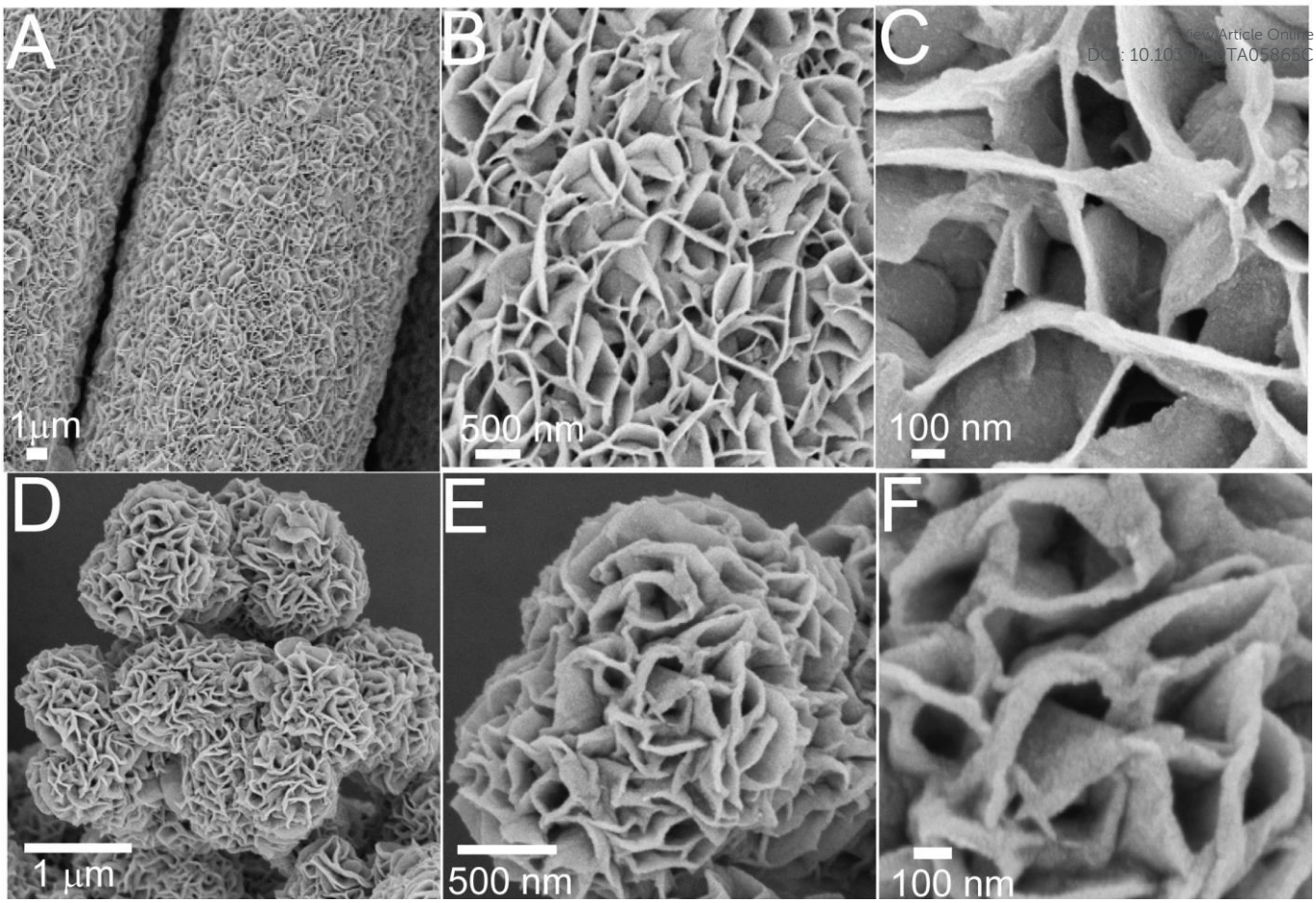

Fig. 1. (A-C) Field emission scanning electron microscopic **(**FE–SEM) images of Ni and P intercalated 1T–enriched MoS_2 nanosheets grown on carbon cloth (1T–$Ni_{0.2}Mo_{0.8}S_{1.8}P_{0.2}$ NS/CC) at different magnifications (low to high). (**D-F**) FE–SEM images of Ni and P intercalated 1T–enriched MoS_2 nanoflowers (1T–$Ni_{0.2}Mo_{0.8}S_{1.8}P_{0.2}$ NFs) at different magnifications.

Field emission scanning electron microscopic **(**FE-SEM) images (**Fig. 1 A-C**) of the 1T-$Ni_{0.2}Mo_{0.8}S_{1.8}P_{0.2}$ NS/CC showed growth of ultrathin 2D-nanosheet structures. FE-SEM images of the control materials, i.e., Ni-MoS_2, P-MoS_2 and MoS_2 grown on carbon cloth (**Fig. S1 A-C, ESI†**), also showed nanosheet structures but length of the sheets was much smaller compared to the 1T-$Ni_{0.2}Mo_{0.8}S_{1.8}P_{0.2}$ NS/CC, indicated formation of superior morphology following doping and intercalation of Ni and P. Similar results was also observed for the 1T-$Ni_{0.2}Mo_{0.8}S_{1.8}P_{0.2}$ powders, the FE-SEM images (**Fig. 1 D-F**) showed the formation of the nanoflowers structures with ultrathin sheets whereas, the FE-SEM images of the control materials i.e., Ni-MoS_2, P-MoS_2 and MoS_2 powders (**Fig. S1 D-F, ESI†**) showed growth of the similar flower-like structures but the length of the edges were much shorter than those of the 1T-$Ni_{0.2}Mo_{0.8}S_{1.8}P_{0.2}$ NFs.

The transmission electron microscopic (TEM, **Fig. 2 A-B**) images and the scanning transmission electron microscopic (STEM, **Fig. 2C**) image of the 1T-$Ni_{0.2}Mo_{0.8}S_{1.8}P_{0.2}$ NS/CC also showed the highly wrinkled and furrowed sheet structures with large surface area. Similarly, the TEM images of the powder 1T-$Ni_{0.2}Mo_{0.8}S_{1.8}P_{0.2}$ NFs showed the flower-like structure (**Fig. 2D**). The TEM images at higher magnifications (**Fig. 2E**) showed a significant increase in the interlayer distances. 1T-$Ni_{0.2}Mo_{0.8}S_{1.8}P_{0.2}$ NFs showed an interlayer spacing of 0.82 nm, a 24% increase from the pristine MoS_2 (0.62nm, **Fig. S2)**.[10] The high resolution TEM image (HR-TEM, **Fig. 2F**) and the corresponding inverse fast Fourier transform (IFFT, **inset**) image showed the lattice fringes with spacing of 0.28 nm matching with (110) plane of the 1T-$Ni_{0.2}Mo_{0.8}S_{1.8}P_{0.2}$, confirming the formation of the same. The selected area electron diffraction (SAED) pattern of the 1T-$Ni_{0.2}Mo_{0.8}S_{1.8}P_{0.2}$ NFs also showed electron diffraction corresponding to the (110) plane of 1T-$Ni_{0.2}Mo_{0.8}S_{1.8}P_{0.2}$ (**Fig. S3, ESI†**).[10] The elemental mapping data of the 1T-$Ni_{0.2}Mo_{0.8}S_{1.8}P_{0.2}$ NFs acquired from TEM (**Fig. 2G**) and FE-SEM (**Fig. S4, ESI†**) confirmed the existence of all the constituent elements, i.e., Mo, S, Ni and P in the nanostructure of the same apparently in the comparable ratio.

X-ray photoelectron spectroscopy (XPS) analysis of the 1T-$Ni_{0.2}Mo_{0.8}S_{1.8}P_{0.2}$ NFs also confirmed the presences of all the constituent elements, namely, Mo, S, Ni and P (**Fig. S5, ESI†**). The high-resolution XPS (HR-XPS) analysis of the Mo 3d showed the occurrence of peaks at 231.5 eV (Mo $3d_{3/2}$) and 228.3 eV (Mo $3d_{5/2}$) corresponding to the 1T-phase and 232.6 eV (Mo $3d_{3/2}$) and 229.3 (Mo $3d_{5/2}$) corresponding to 2H-phase

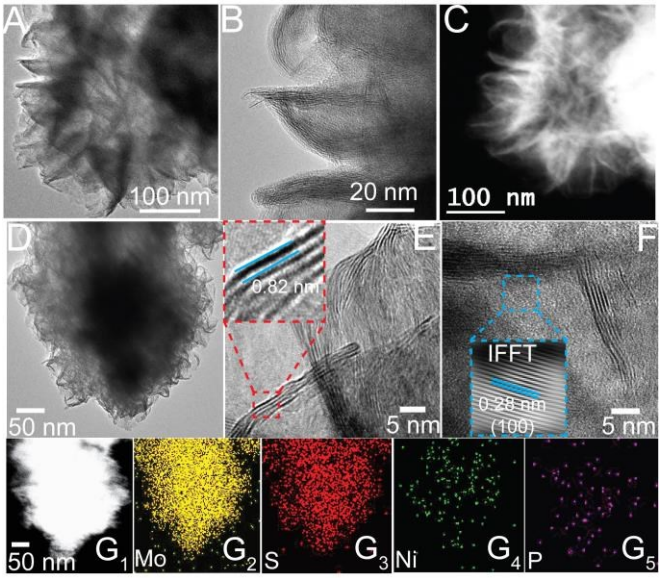

Fig. 2. (**A-B**) Transmission electron microscopic (TEM) images of 1T-$Ni_{0.2}Mo_{0.8}S_{1.8}P_{0.2}$ NS/CC at different magnifications. (**C**) Scanning transmission electron microscopic (STEM) image of 1T-$Ni_{0.2}Mo_{0.8}S_{1.8}P_{0.2}$ NS/CC. (**D**) TEM image of 1T-$Ni_{0.2}Mo_{0.8}S_{1.8}P_{0.2}$ NFs. (**E**) Corresponding TEM images at higher magnification showing the inter-layer spacing with distances of ~0.82 nm. (**F**) High-resolution TEM image and (**inset**) showing the lattice fringes corresponding to the (100) plane of 1T-$Ni_{0.2}Mo_{0.8}S_{1.8}P_{0.2}$ NFs. (**G**) Elemental mapping of 1T-$Ni_{0.2}Mo_{0.8}S_{1.8}P_{0.2}$ NFs showing the presences of individual elements; (**G_1**) STEM image, (**G_2**) molybdenum (Mo) (**G_3**) sulfur (S) (**G_4**) nickel (Ni) (**G_5**) phosphorous (P).

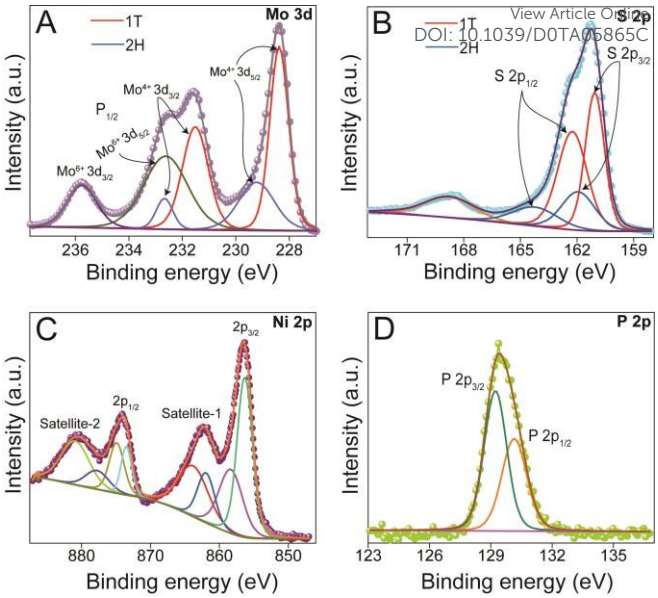

Fig. 3. High-resolution XPS spectrum of (**A**) Mo 3d, (**B**) S 2p, (**C**) Ni 2p, and (**D**) P 2p for 1T-$Ni_{0.2}Mo_{0.8}S_{1.8}P_{0.2}$.

(**Fig. 3A**).[13–17] In both cases, Mo $3d_{3/2}$ and Mo $3d_{5/2}$, peak intensities for the 1T-phase are much higher compared to the 2H-phase, indicating enrichment of the1T-phase of $Ni_{0.2}Mo_{0.8}S_{1.8}P_{0.2}$ in the 2D nanostructures. Other peaks corresponding to Mo^{6+} $3d_{3/2}$ (235.8 eV) and Mo^{6+} $3d_{5/2}$ (232.8 eV) were also observed (**Fig. 3A**). HR-XPS analysis of S 2p spectrum (**Fig. 3B**) showed the presence of peaks at 164.6 eV (S $2p_{3/2}$) and 161.9 eV (S $2p_{1/2}$) corresponding to the 2H-phase of $Ni_{0.2}Mo_{0.8}S_{1.8}P_{0.2}$ and 162.8 eV (S $2p_{3/2}$) and 161.1 eV (S $2p_{1/2}$) corresponding to the 1T-phase of $Ni_{0.2}Mo_{0.8}S_{1.8}P_{0.2}$.[13–17] In this case, also the intensity of the peaks for 1T-phase is much higher compared to the 2H-phase, confirming the formation of 1T-$Ni_{0.2}Mo_{0.8}S_{1.8}P_{0.2}$. The HR-XPS analysis of Ni 2p also showed the presence of characteristic peaks regarding Ni $2p_{1/2}$ and Ni $2p_{3/2}$ in the range from 850 to 885 eV (**Fig. 3C**), confirming the doping of Ni.[7,21,27–29] The HR-XPS analysis of P 2p (**Fig. 3D)** showed the presence of peaks at 129.2 eV and 130.1 eV corresponding to $2p_{1/2}$ and $2p_{3/2}$ of the phosphorus, confirming the doping of P on 1T-$Ni_{0.2}Mo_{0.8}S_{1.8}P_{0.2}$ NFs.[7,10,20] XPS analysis of the pristine MoS_2 was also carried out, HR-XPS of the Mo 3d and S 2p peaks showed predominance of the 2H phase (**Figure S6**). HR-XPS analysis Mo 3d showed peaks corresponding to Mo^{6+} $3d_{3/2}$, Mo^{6+} $3d_{5/2}$, Mo^{4+} $3d_{3/2}$ and Mo^{4+} $3d_{5/2}$ at 235.7 eV, 232.9 eV, 232.4eV and 229.2 eV corresponding to 2H-MoS_2 and HR-XPS analysis S 2p showed peaks at 164.5 eV (S $2p_{3/2}$) and 162.1 eV (S $2p_{1/2}$) corresponding to the 2H-MoS_2 (**Figure S6**). Thus, from the XPS study of $Ni_{0.2}Mo_{0.8}S_{1.8}P_{0.2}$ and pristine MoS_2, we can conclude the existence of all the constituent elements in their respective oxidation states and the enrichment of the1T-phase.[7,10,20,23,25,27,39]

The superior morphological nature was further validated from the high surface area and porosity obtained from the N_2 adsorption-desorption isotherms. The data showed 1T-$Ni_{0.2}Mo_{0.8}S_{1.8}P_{0.2}$ NFs has very high surface area ~83 m^2 g^{-1} with average pore diameter ~14 nm (**Fig. 4A**), whereas control materials i.e., MoS_2, Ni-MoS_2 and P-MoS_2 nanoflowers showed much lower surface area ~46 m^2 g^{-1}, 52 m^2 g^{-1} and 61 m^2 g^{-1} respectively (**Fig. S7**, **ESI†**). The formation of the superior morphology of 1T-$Ni_{0.2}Mo_{0.8}S_{1.8}P_{0.2}$ compared to the other controlled materials is mainly due to the competitive bond formation possibility between like and unlike elements in the reaction environment. Moreover the, presence of Ni and P induces strain in the nano seeds of the MoS_2 formed during the very initial phase of the reaction and thus, will alter the growth mechanism of the nanostructures.[7,10,20,23,25,27,39] 1T-$Ni_{0.2}Mo_{0.8}S_{1.8}P_{0.2}$ NS/CC also showed very high surface area ~91 m^2 g^{-1} with average pore diameter ~17 nm (**Fig. 4A**).The powder X-ray diffraction (XRD) pattern study of the 1T-$Ni_{0.2}Mo_{0.8}S_{1.8}P_{0.2}$ NFs was carried out to investigate the crystallographic nature of the material (**Fig. 4B**). Results showed a slight shift of the (002) peak from 14.4° to 14.2° due to formation of the 1T-phase as reported in many previous literatures.[13,14,31,32] Other peaks, at 2θ = 32.8°, 33.5°, 39.7°, 44.0° and 49.9° corresponding to the (100), (101), (103), (006) and (105) are also present, confirming the formation of the 1T-$Ni_{0.2}Mo_{0.8}S_{1.8}P_{0.2}$ NFs (**Fig. 4B**).[13,14,31,32] Diffraction peaks regarding (106), (110), (008), (107) planes is appeared as merged to give a broad pattern due to the close proximity of the peaks and the nanosheet structure of the material, this broad nature is found in many other reports also.[10,13,14,21,31,32] Overall, the XRD analysis provided evidences of the formation of 1T-$Ni_{0.2}Mo_{0.8}S_{1.8}P_{0.2}$ NFs. Raman study of 1T-$Ni_{0.2}Mo_{0.8}S_{1.8}P_{0.2}$

View Article Online
DOI: 10.1039/D0TA05865C

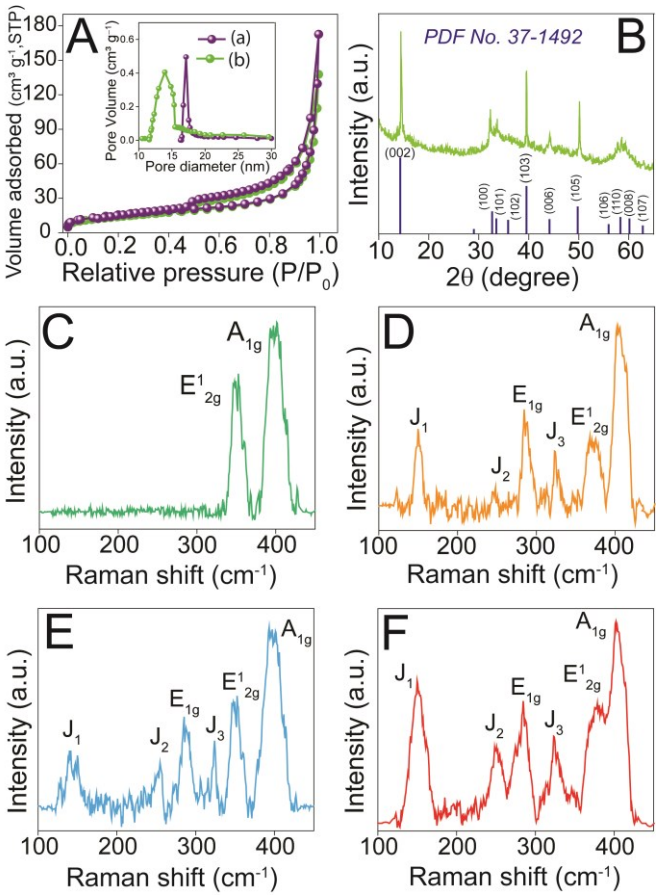

Fig. 4. (**A**) N_2 adsorption-desorption isotherms of (a) 1T-$Ni_{0.2}Mo_{0.8}S_{1.8}P_{0.2}$ NS/CC and (b) 1T-$Ni_{0.2}Mo_{0.8}S_{1.8}P_{0.2}$ NFs showing type IV hysteresis loop, (**Inset**) pore size distribution of 1T-$Ni_{0.2}Mo_{0.8}S_{1.8}P_{0.2}$ NS/CC and 1T-$Ni_{0.2}Mo_{0.8}S_{1.8}P_{0.2}$ NFs. (**B**) X-ray powder diffraction (XRD) pattern of 1T-$Ni_{0.2}Mo_{0.8}S_{1.8}P_{0.2}$ NFs. Raman spectra of (**C**) MoS_2 (**D**) P-MoS_2 (**E**) Ni-MoS_2 and (**F**) 1T-$Ni_{0.2}Mo_{0.8}S_{1.8}P_{0.2}$ NFs.

NFs (**Fig. 4F**) showed the peaks at 151, 249, 284, 324, 380, and 402 cm^{-1} corresponding to the Raman modes J_1, J_2, E_{1g}, J_3, E^1_{2g}, and A_{1g}, conclusively proving the enrichment of the 1T-phase of $Ni_{0.2}Mo_{0.8}S_{1.8}P_{0.2}$. The Raman spectrum of pristine MoS_2 (**Fig. 4C**) showed the formation predominantly 2H-phase with the presence of E^1_{2g}, and A_{1g} peaks, thus, indicating the role of the Ni and P doping for the formation of the 1T-phase in $Ni_{0.2}Mo_{0.8}S_{1.8}P_{0.2}$. Raman spectra of P-doped and Ni-doped MoS_2 (**Fig. 4 D, E**) also showed partial stabilization of the 1T-phase with the existence of the Raman modes specific to the metallic phase.[7,21,27–29] However, the nature of the spectrum and intensity of those peaks are relatively less matured compared to the1T-$Ni_{0.2}Mo_{0.8}S_{1.8}P_{0.2}$.

Electrocatalytic performance

The catalytic activity of the 1T-$Ni_{0.2}Mo_{0.8}S_{1.8}P_{0.2}$ NS/CC and 1T-$Ni_{0.2}Mo_{0.8}S_{1.8}P_{0.2}$ NFs catalysts towards the hydrogen evolution reaction (HER) was carried out in a three-electrode system using 1 M KOH (N_2-saturated) as the electrolyte, Ag/AgCl as the reference electrode, and graphite rod as a counter electrode. 1T-$Ni_{0.2}Mo_{0.8}S_{1.8}P_{0.2}$ NFs catalysts was coated on the CC (1 cm^2) using nafion–117 as binder (details in **experimental section**) and used as working electrode whereas the freestanding 1T-$Ni_{0.2}Mo_{0.8}S_{1.8}P_{0.2}$ NS/CC was directly used as an electrode of size 1 cm^2. The linear–sweep voltammetry (LSV) data were obtained at a scan rate of 2 mV s^{-1} and polarization curves as–obtained from LSV after iR–correction are plotted in **Fig. 5A.** 1T-$Ni_{0.2}Mo_{0.8}S_{1.8}P_{0.2}$ NS/CC showed that the overpotential (η_{HER}) required to reach the current densities of 10 mA cm^{-2} and 50 mAcm^{-2} was ~55mV and 180 mV respectively. The η_{HER} values for 1T-$Ni_{0.2}Mo_{0.8}S_{1.8}P_{0.2}$ NFs was found to be ~99mV and 223 mV to reach current densities of 10 mA cm^{-2} and 50 mAcm^{-2}, respectively. Whereas the required overpotential observed for standard Pt/C catalyst to reach the same current densities was ~11 mV and 84 mV. Similar experiments were carried out using the other control materials, i.e., MoS_2, Ni-MoS_2, and P-MoS_2, as catalysts to find out the superior nature of the 1T-$Ni_{0.2}Mo_{0.8}S_{1.8}P_{0.2}$ towards HER. The results (**Fig. 5A**) showed MoS_2, Ni-MoS_2 and P-MoS_2, required an overpotential of ~257, 191, and 146 mV to reach a current density of 10 mA cm^{-2} and ~408, 364, 277 mV to reach current density of 50 mA cm^{-2}, respectively. Bare CC was also investigated, and it was observed that it does not has any significant catalytic activity indicating negligible contribution of the current collector during the efficacy measurements of the catalysts (**Fig. 5A**). The above discussions showed that the onset-potential and the overpotential was found in the following order Pt/C<1T-$Ni_{0.2}Mo_{0.8}S_{1.8}P_{0.2}$ NS/CC<1T-$Ni_{0.2}Mo_{0.8}S_{1.8}P_{0.2}$ NFs<P-doped MoS_2<Ni-doped MoS_2<MoS_2<CC, and the overpotential values for the as-synthesized catalysts are quite impressive and better than the contemporary reported materials (**Fig. 5A and B, Table S2, ESI†**). This result indicated that the expansion in the interlayer spacing, activation of the basal–planes, enrichment of the 1-T phase and the formation of nanostructures with ultrathin edges following intercalation and doping of Ni and P has greatly influenced the HER catalytic performance of the 1T-$Ni_{0.2}Mo_{0.8}S_{1.8}P_{0.2}$.[7,10,20,23,25,27,39] Materials with other doping ratios of Ni and P i.e., $Ni_{0.2}Mo_{0.8}S_{1.7}P_{0.3}$, $Ni_{0.2}Mo_{0.8}S_{1.9}P_{0.1}$ $Ni_{0.3}Mo_{0.7}S_{1.7}P_{0.3}$, $Ni_{0.3}Mo_{0.7}S_{1.8}P_{0.2}$, $Ni_{0.3}Mo_{0.7}S_{1.9}P_{0.1}$ $Ni_{0.1}Mo_{0.9}S_{1.8}P_{0.2}$, $Ni_{0.1}Mo_{0.9}S_{1.7}P_{0.3}$, $Ni_{0.1}Mo_{0.9}S_{1.9}P_{0.1}$, showed the lower HER catalytic efficacy compared to 1T-$Ni_{0.2}Mo_{0.8}S_{1.8}P_{0.2}$ with η_{HER} ~113, mV 119 mV, 122 mV, 136 mV, 138 mV, 139 mV, 157 mV and 175 mV to reach a current density of 10 mA cm^{-2} (**Fig. S8A**). The kinetic involved in the catalytic reaction of the above-mentioned catalysts were explored using Tafel plot analysis (**Fig. 5C**). The analysis showed the slope value was lowest in case of 1T-$Ni_{0.2}Mo_{0.8}S_{1.8}P_{0.2}$ NS/CC (***NPMS-CC,*** 66.1 mV dec^{-1}) among all the as-synthesized catalysts i.e., 1T-$Ni_{0.2}Mo_{0.8}S_{1.8}P_{0.2}$ NFs (***NPMS-NFs,*** 72.3 mV dec^{-1}), MoS_2 (163.1 mV dec^{-1}), Ni-MoS_2 (136.4 mV dec^{-1}), and P-MoS_2 (93.7 mV dec^{-1}). However, the slope value is higher compared to standard Pt-C (52.7 mV dec^{-1}) catalyst. The bare CC showed much higher Tafel slope 223.6 mV dec^{-1} compared to all the other catalysts, indicating negligible contribution of it.

Little higher value of η_{HER} and Tafel slope for 1T-$Ni_{0.2}Mo_{0.8}S_{1.8}P_{0.2}$ NFs was observed compared to 1T-$Ni_{0.2}Mo_{0.8}S_{1.8}P_{0.2}$ NS/CC is due to the presence of the

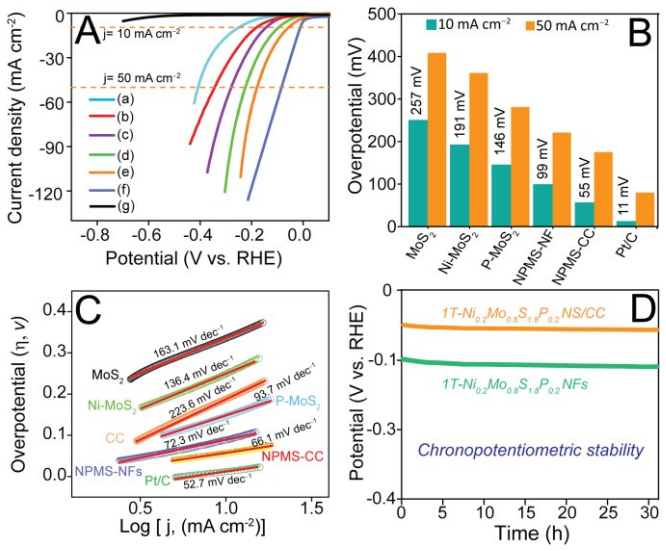

Fig. 5. (**A**) Linear–sweep voltammetry (LSV) measurements for hydrogen evolution reaction (HER) in 1 (M) KOH of (**a**) MoS_2 (**b**) Ni-doped MoS_2 (**c**) P-doped MoS_2 (**d**) 1T-$Ni_{0.2}Mo_{0.8}S_{1.8}P_{0.2}$ NFs (***NPMS-NFs***) (**e**) 1T-$Ni_{0.2}Mo_{0.8}S_{1.8}P_{0.2}$ NS/CC (***NPMS-CC***) (**f**) Pt-C (**g**) Bare carbon cloth (CC). (**B**) HER-overpotential comparison plot of different materials at the current densities of 10 mA cm^{-2} and 50 mA cm^{-2}. (**C**) Tafel plots of corresponding electrocatalysts. (**D**) Chronopotentiometry stability test of 1T-$Ni_{0.2}Mo_{0.8}S_{1.8}P_{0.2}$ NFs and 1T-$Ni_{0.2}Mo_{0.8}S_{1.8}P_{0.2}$ NS/CC.

catalytically inactive binder nafion–117 during the fabrication of the 1T-$Ni_{0.2}Mo_{0.8}S_{1.8}P_{0.2}$ NFs electrode via ink preparation method, however, due to possibility of a large-scale synthesis potential and considerably high electrocatalytic activity of 1T-$Ni_{0.2}Mo_{0.8}S_{1.8}P_{0.2}$ NFs for satisfying the industrial need, we have considered it in the present study. Overall, the above results indicate that 1T-$Ni_{0.2}Mo_{0.8}S_{1.8}P_{0.2}$ showed a significant improvement in the catalytic reaction kinetics over others towards HER. The slope value in the Tafel plot indicated that the 1T-$Ni_{0.2}Mo_{0.8}S_{1.8}P_{0.2}$ catalyst followed Volmer-Heyrovsky HER mechanism.[37,38] This reaction occurred in two separate steps, as follows; [37,38]

The Volmer step:

$H_2O + M^* + e^- \Leftrightarrow M^* - H_{ads} + OH^-$ ..... (1)

The Heyrovsky step:

$H_2O + M^* - H_{ads} + e^- \Leftrightarrow H_2 + M^* + OH^-$..... (2)

For the other materials, MoS_2, Ni-MoS_2, and P-MoS_2 the slope value is much higher, as mentioned above, indicating a very slow progress of the rate determining Volmer step.[37,38,40] As the reaction mechanism is strongly dependent on the electronic structure and surface chemistry of the materials, doping of Ni and P together has strongly influenced both the parameters; hence, a significant improvement in the catalytic efficacy of the material is observed in the present study. Basically, presence of large numbers of active basal planes and ultrathin edges in a highly conductive MoS_2 with expanded interlayer spacing produces best possible HER performances which was further validated following electrochemically active surface area (ECSA) measurements. ECSA can be determined using following equation ECSA=C_{dl}/C_s, where C_s is the specific capacitance of flat surface and C_{dl} is the electrochemical double layer capacitance. The ECSA value is directly proportional to C_{dl} and the C_{dl} value and was highest for 1T-$Ni_{0.2}Mo_{0.8}S_{1.8}P_{0.2}$ NS/CC (~10.5 mF cm^{-2}) and follows the order 1T-$Ni_{0.2}Mo_{0.8}S_{1.8}P_{0.2}$ NFs (~9.5 mF cm^{-2})>P-MoS_2 (~7 mF cm^{-2})>Ni-MoS_2 (~4.5 mF cm^{-2})>MoS_2 (~2.5 mF cm^{-2}) (**Fig. S9, ESI†**). The impedance Spectroscopy (EIS) measurements (**Fig. S10, ESI†**) shows that the charge–transfer resistance (R_{ct}) follows the order; 1T-$Ni_{0.2}Mo_{0.8}S_{1.8}P_{0.2}$ NS/CC <1T-$Ni_{0.2}Mo_{0.8}S_{1.8}P_{0.2}$ NFs< Ni-MoS_2<P-MoS_2 <MoS_2 (**Fig. S10, ESI†**). The lowest R_{ct} value for 1T-$Ni_{0.2}Mo_{0.8}S_{1.8}P_{0.2}$ indicated the fastest electron-transfer reaction in the electrode-electrolyte interface due to increase in conductivity of MoS_2 following doping and intercalation of Ni and P. The long-term stability of a catalyst is another very important factor for its commercial use. The stability of the 1T-$Ni_{0.2}Mo_{0.8}S_{1.8}P_{0.2}$ NFs was first tested with 1,000 consecutive CV cycles followed by LSV measurements. The results showed no significant change in the characteristic of the LSV curve (**Fig. S11, ESI†**). The robustness of 1T-$Ni_{0.2}Mo_{0.8}S_{1.8}P_{0.2}$ catalysts was also tested using chronopotentiometry at a fixed current of 10 mA cm^{-2} 33 h (**Fig. 5D**) and the potential showed only 2% degradation in the initial potential for 1T-$Ni_{0.2}Mo_{0.8}S_{1.8}P_{0.2}$ NFs and 1% for 1T-$Ni_{0.2}Mo_{0.8}S_{1.8}P_{0.2}$ NS/CC, confirming the superior nature of the materials. Moreover, the LSV measurement after the completion of the chronopotentiometric stability test also did not show any significant change (**Fig. S11, ESI†**). Together, these results indicate superior efficacy of the catalysts with very high robustness.

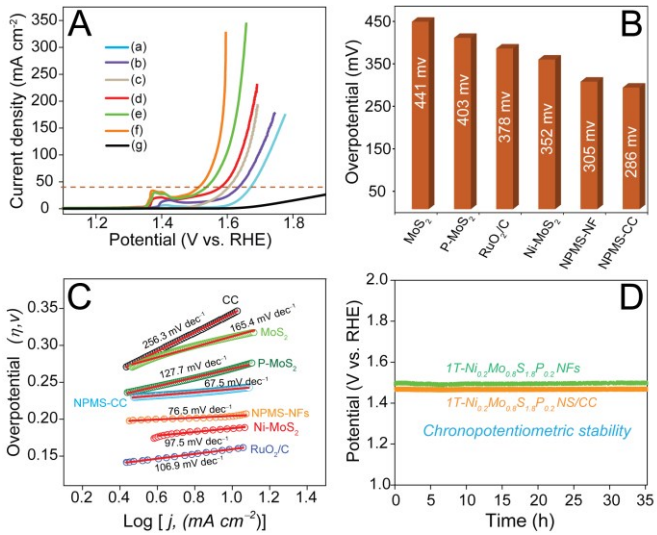

Fig. 6. (A) Linear–sweep voltammetry (LSV) measurements towards oxygen evolution reaction (OER) in 1 (M) KOH of (**a**) MoS_2 (**b**) P-doped MoS_2 (**c**) RuO_2–C (**d**) Ni-doped MoS_2 (**e**) 1T–$Ni_{0.2}Mo_{0.8}S_{1.8}P_{0.2}$ NFs (***NPMS–NFs***) (**f**) 1T–$Ni_{0.2}Mo_{0.8}S_{1.8}P_{0.2}$ NS/CC (***NPMS–CC***) and (**g**) Bare carbon cloth (CC). (**B**) OER–overpotentials comparison plot of different materials at the current density of 40 mA cm^{-2}. (**C**) Tafel plots of corresponding electrocatalysts (**D**) Chronopotentiometry stability test of 1T–$Ni_{0.2}Mo_{0.8}S_{1.8}P_{0.2}$ NFs and 1T–$Ni_{0.2}Mo_{0.8}S_{1.8}P_{0.2}$ NS/CC.

The catalytic efficiency of all the materials, i.e., 1T-$Ni_{0.2}Mo_{0.8}S_{1.8}P_{0.2}$, MoS_2, Ni-MoS_2 and P-MoS_2 towards the oxygen evolution reaction (OER) was also carried out in a similar three-electrode system using 1(M) KOH solution as the electrolyte. LSV of all the materials was measured at the same scan rate of 2 mV s^{-1} using a graphite rod as the counter

View Article Online
DOI: 10.1039/D0TA05865C

electrode, Ag/AgCl as the reference electrode and 1 cm^2 size of the prepared electrocatalysts as working electrode. The OER overpotential (η_{OER}) was calculated using the following formula $\eta = E_{RHE} - 1.23V$. The results (**Fig. 6A,B**) showed, overpotentials required to reach the current density of 40 mA cm^{-2} are 286 mV, 305 mV, 352 mV, 378 mV, 403 mV and 441 mV for 1T-$Ni_{0.2}Mo_{0.8}S_{1.8}P_{0.2}$ NS/CC (***NPMS-CC)***, 1T-$Ni_{0.2}Mo_{0.8}S_{1.8}P_{0.2}$ NFs (***NPMS-NFs)***, Ni-MoS_2, RuO_2, P-MoS_2 and MoS_2 respectively. Whereas bare CC showed negligible catalytic activity. Materials with other doping ratios of Ni and P i.e., $Ni_{0.1}Mo_{0.9}S_{1.8}P_{0.2}$, $Ni_{0.3}Mo_{0.7}S_{1.8}P_{0.2}$, $Ni_{0.2}Mo_{0.8}S_{1.7}P_{0.3}$, $Ni_{0.2}Mo_{0.8}S_{1.9}P_{0.1}$, $Ni_{0.1}Mo_{0.9}S_{1.7}P_{0.3}$, $Ni_{0.1}Mo_{0.9}S_{1.9}P_{0.1}$, $Ni_{0.3}Mo_{0.7}S_{1.7}P_{0.3}$, $Ni_{0.3}Mo_{0.7}S_{1.9}P_{0.1}$ showed the lower OER catalytic efficacy compared to 1T-$Ni_{0.2}Mo_{0.8}S_{1.8}P_{0.2}$ with η_{OER} ~322, mV 329 mV, 337 mV, 339 mV, 342 mV, 348 mV, 364 mV and 382 mV to reach a current density of 40 mA cm^{-2} respectively **(Fig. S8B)**. The 40 mA cm^{-2} current density was chosen to avoid the redox contribution of the materials. As expected, the 1T-$Ni_{0.2}Mo_{0.8}S_{1.8}P_{0.2}$ showed much lower overpotentials/onset-potentials compared to others, the value was even much lower compared to the RuO_2-C (a well-known OER catalyst), indicating the high efficiency of the materials towards efficient OER reaction. The kinetics of the OER reaction were further evaluated using Tafel plot analysis (**Fig. 6C**). The Tafel slope value for 1T-$Ni_{0.2}Mo_{0.8}S_{1.8}P_{0.2}$ NS/CC (***NPMS-CC)***, 1T-$Ni_{0.2}Mo_{0.8}S_{1.8}P_{0.2}$ NFs (***NPMS-NFs)***, MoS_2, Ni-MoS_2, P-MoS_2, and RuO_2-C was 67.5 mV dec^{-1}, 76.5 mV dec^{-1}, 165.4 mV dec^{-1}, 97.5 mV dec^{-1}, 127.7 mV dec^{-1} and 106.9 mV dec^{-1} respectively (**Fig. 6C)**. The slope value was found to be lowest in 1T-$Ni_{0.2}Mo_{0.8}S_{1.8}P_{0.2}$ among all the synthesized materials. 1T-$Ni_{0.2}Mo_{0.8}S_{1.8}P_{0.2}$ NS/CC showed 38.8 mV dec^{-1} lower values compared to the commonly used OER catalyst RuO_2-C, whereas, 1T-$Ni_{0.2}Mo_{0.8}S_{1.8}P_{0.2}$ NFs showed 30.4 mV dec^{-1} lower values RuO_2-C. The above results suggested the significant improvement in the OER catalytic efficacy of pristine MoS_2 following intercalation and doping of Ni and P. This improvement is due to five main reasons, *(i) activation of the basal plane (ii) enrichment in the 1T phase (iii) expansion of interlayer spacing (iv) improvement in morphology and increase in surface area (iv) generation of additional active Ni-centers for OER catalysis.* The increase in ECSA as ascertained from calculating C_{dl} (**Fig. S9, ESI†**) and the decrease in R_{ct} (**Fig. S10, ESI†**) also suggested superior electrochemical behavior of 1T-$Ni_{0.2}Mo_{0.8}S_{1.8}P_{0.2}$. The ECSA normalized LSV results were also calculated and plotted in the **Fig. S12** which showed similar trend to that of **Fig6A**, implying that the improvement in the catalytic-OER activity is due to change in the intrinsic properties of the MoS_2 due to Ni and P doping. The long-term stability of the 1T-$Ni_{0.2}Mo_{0.8}S_{1.8}P_{0.2}$ catalyst towards OER is another most important factor for commercial use of a catalyst and was evaluated following chronopotentiometry and CV cycles. After the 1,000th consecutive CV measurement, no significant change in the LSV curve of 1T-$Ni_{0.2}Mo_{0.8}S_{1.8}P_{0.2}$ NFs was observed (**Fig. S13, ESI†**), indicating the stable nature of the catalyst towards OER. Further, the chronopotentiometric stability test was carried out at a fixed current density of 40 mA cm^{-2} for 35 h (**Fig. 6D**). The result showed excellent long term durability for 1T-$Ni_{0.2}Mo_{0.8}S_{1.8}P_{0.2}$ NFs and 1T-$Ni_{0.2}Mo_{0.8}S_{1.8}P_{0.2}$ NS/CC indicated by a slight increase ~2% and 3% in their initial overpotential values, respectively. The LSV curve after finishing the chronopotentiometric stability test also did not deviate significantly, indicating the ultrahigh stability of the catalyst towards OER (**Fig. S13, ESI†**). So, overall, the above results established 1T-$Ni_{0.2}Mo_{0.8}S_{1.8}P_{0.2}$ as a superior electrocatalyst for OER and the efficacy was comparable to that of the contemporary reported materials (**Table S3, ESI†**), establishing 1T-$Ni_{0.2}Mo_{0.8}S_{1.8}P_{0.2}$ a highly efficient and robust novel electrocatalysts for OER.

Overall water splitting study

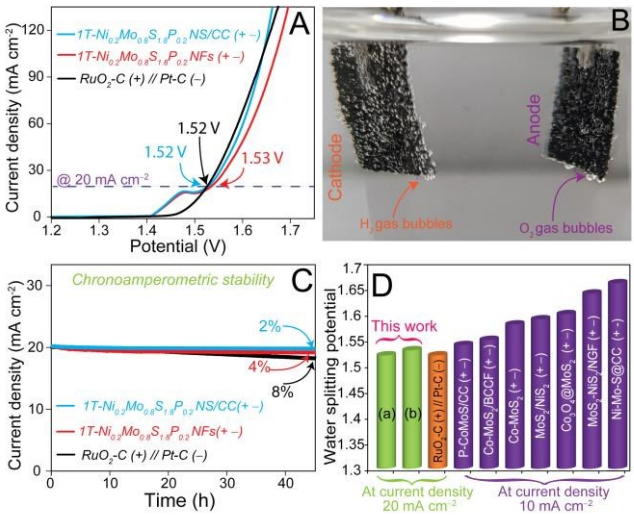

Fig. 7. (A) LSV curves of 1T-$Ni_{0.2}Mo_{0.8}S_{1.8}P_{0.2}$ NS/CC (+ -), 1T-$Ni_{0.2}Mo_{0.8}S_{1.8}P_{0.2}$ NFs (+ -) and RuO_2-C (+) // Pt-C (-) devices for water electrolysis at scan rate of 2 mV s^{-1} in 1.0 M KOH electrolyte. (**B**) Digital image of the1T-$Ni_{0.2}Mo_{0.8}S_{1.8}P_{0.2}$ NFs (+ -) device during water electrolysis reaction showing the emergence of H_2 and O_2 gas bubbles on the surface of the cathode and anode. (**C**) Chronoamperometric durability test of the 1T-$Ni_{0.2}Mo_{0.8}S_{1.8}P_{0.2}$ NS/CC (+ -), 1T-$Ni_{0.2}Mo_{0.8}S_{1.8}P_{0.2}$ NFs (+ -) and RuO_2-C (+) // Pt-C (-) devices for 45h. (**D**) Comparison table of cell voltages for overall water splitting of (a)1T-$Ni_{0.2}Mo_{0.8}S_{1.8}P_{0.2}$ NS/CC (+ -) (b) 1T-$Ni_{0.2}Mo_{0.8}S_{1.8}P_{0.2}$ NFs (+ -) devices with RuO_2-C (+) // Pt-C (-) device, and recently reported molybdenum-based materials.

Based on the results obtained from the three-electrode system for HER and OER, it can be concluded that 1T-$Ni_{0.2}Mo_{0.8}S_{1.8}P_{0.2}$ has the potential to function as both cathode and anode for an efficient overall water splitting reaction.

The efficacy of the present materials for the overall water splitting was tested using 1 M KOH as electrolyte and plotted in **Fig. 7A.** A control experiment for reference was also performed using commercially available RuO_2-C as anode and Pt-C as the cathode. The results showed an excellent water splitting efficiency for the 1T-$Ni_{0.2}Mo_{0.8}S_{1.8}P_{0.2}$ NS/CC (+ -) device with a cell potential of only 1.52 V at current density of 20 mA cm^{-2}. The water-splitting potential value was found identical to that of commercially used RuO_2-C (+) // Pt-C (-) system at the same current density, and at very high current density the 1T-$Ni_{0.2}Mo_{0.8}S_{1.8}P_{0.2}$ NS/CC (+ -) system shows slightly better performance indicating superior nature of the

View Article Online
DOI: 10.1039/D0TA05866C

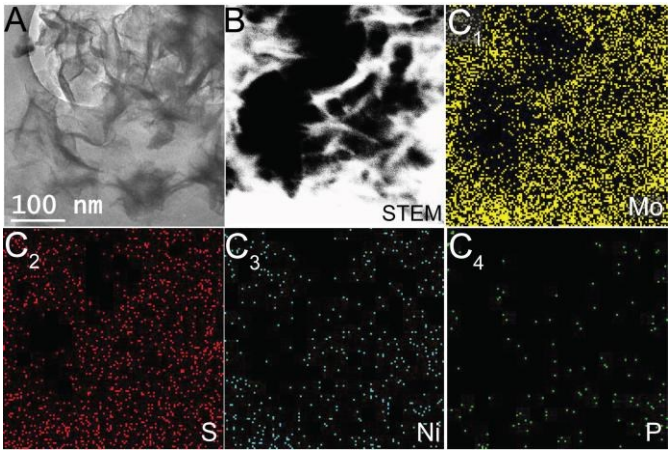

Fig. 8. (A) TEM image. (B) STEM image. (C) Corresponding elemental mapping; C_1, C_2, C_3, and C_4 representing Mo, S, Ni and P, respectively of 1T-$Ni_{0.2}Mo_{0.8}S_{1.8}P_{0.2}$ NS/CC after long-term chronoamperometric stability test of the device showing no significant change in the structure and composition of the catalyst.

1T-$Ni_{0.2}Mo_{0.8}S_{1.8}P_{0.2}$ NS/CC catalyst (**Fig. 7A**). The 1T-$Ni_{0.2}Mo_{0.8}S_{1.8}P_{0.2}$ NFs (+ -) device also showed only a marginally compromised performance compared to that of the 1T-$Ni_{0.2}Mo_{0.8}S_{1.8}P_{0.2}$ NS/CC (+ -) system due to presence of the catalytically inactive nafion–117 binder to the powder sample for the preparation of the electrodes. 1T-$Ni_{0.2}Mo_{0.8}S_{1.8}P_{0.2}$ NFs (+ -) system showed the required cell potential of 1.53 V for overall water splitting to reach the current density of 20 mA cm^{-2}. The digital images of the 1T-$Ni_{0.2}Mo_{0.8}S_{1.8}P_{0.2}$ NFs (+ -) device clearly showing the generation of H_2 and O_2 gas bubbles on the electrode surface (**Fig. 7B**). Finally, the chronoamperometric stability test of the devices was done at a current density of 20 mA cm^{-2} **(Fig. 7C)**. The results showed that both 1T-$Ni_{0.2}Mo_{0.8}S_{1.8}P_{0.2}$ NFs (+ -) and 1T-$Ni_{0.2}Mo_{0.8}S_{1.8}P_{0.2}$ NS/CC (+ -) devices showed slightly better durability compared to the RuO_2-C (+) // Pt-C (-) device. The 1T-$Ni_{0.2}Mo_{0.8}S_{1.8}P_{0.2}$ NS/CC (+ -) device showed the best durability among all and showed only 2% reduction in the current density over 45h time, whereas 1T-$Ni_{0.2}Mo_{0.8}S_{1.8}P_{0.2}$ NFs (+ -) showed a 4% degradation of the initial current density over the same period of time and RuO_2-C (+) // Pt-C (-) device showed an 8% degradation in similar set of conditions. Overall, the catalytic efficacy shown by the present the 1T-$Ni_{0.2}Mo_{0.8}S_{1.8}P_{0.2}$ NFs (+ -) and 1T-$Ni_{0.2}Mo_{0.8}S_{1.8}P_{0.2}$ NS/CC (+ -) systems are found superior over the recently reported Mo-based materials (**Fig. 7D**), specifically because all the possible driving factors, like enrichment of the metallic 1T-phase, interlayer spacing, activation of the basal planes, fabrication of nanostructures with ultrathin edges and was optimally tuned to get best water catalytic efficacy of MoS_2. Moreover, the efficiency was also found much superior compared to the contemporary reports of electrocatalyst based on other transition metals chalcogenides (**Table S4, ESI†**). Finally, the robustness of the material for electrocatalysis was further tested flowing post-stability TEM, FESEM, XRD and XPS analysis. TEM image (**Fig. 8A**) and FESEM images (**Fig. S14 A**) of the 1T-$Ni_{0.2}Mo_{0.8}S_{1.8}P_{0.2}$ NS/CC after chronoamperometric stability test showed no significant changes in the morphological sheet structure of the catalyst. Further, STEM images and corresponding elemental mapping (**Fig. 8 B-C**) and elemental mapping obtained from FESEM-EDX (**Fig. S14 B-G**) also showed the similar elemental composition with the as synthesized one, confirming no significant change in the elemental compositions. Comparable results were also observed from XRD pattern of the $Ni_{0.2}Mo_{0.8}S_{1.8}P_{0.2}$ post chronoamperometric stability test, result does not show any significant changes compared to the as synthesized one (**Fig. S 15**). Moreover, HR-XPS analysis of Mo 3d, S 2p and Ni 2p peak of the catalyst post chronoamperometric stability test does not show any significant changes of the corresponding peak position compared to the as synthesized one (**Fig. S 16 A-C**). However, HR-XPS peak of P 2p was observed at 134.1 eV and 133.2 eV corresponding to 2 $P_{1/2}$ and 2 $P_{3/2}$ of PO_4^{-3} (**Fig. S 16 D**), different from the as synthesized one, this could be because of the surface oxidation of the P present in the catalyst.[7,10,20,23,25,27,39] All the above results together confirming robust morphological, crystallographic, and chemical stability of the material for reusable industrial use.

Conclusion

In summary, we have demonstrated fabrication of a MoS_2 based highly efficient electrocatalyst for overall water splitting following synchronous inclusion of all the possible driving factors; *(i) enrichment in 1T-phase (ii) expansion of interlayer spacing (iii) activation of the basal planes (iv) development of nanostructures with ultra-thin edges* for highest electrocatalytic efficacy of MoS_2 following co-doping of Ni and P. Enrichment of the 1T-phase was found following synchronous doping of Ni and P, where both the elements develop lattice strain to the host phase and Ni acts as an electron donor too for the stabilization of the1T-$Ni_{0.2}Mo_{0.8}S_{1.8}P_{0.2}$. Both 1T-$MoS_2$ and P-doped MoS_2 has active basal planes, thus, doping of P on 1T-MoS_2 has led to the activation of significantly larger number of basal planes for electrocatalytic water splitting, which was validated from substantial enhancement in the both HER and OER performance. 1T-$Ni_{0.2}Mo_{0.8}S_{1.8}P_{0.2}$ also has expanded the interlayer spacing by 24%, which facilitated smooth directional passage of the electrolyte and provides more active sites to interact with the electrolyte. Ni, alongside of stabilizing the 1-T phase also alter electron density around Mo thus, combination with other factors reduces the hydrogen and oxygen adsorption free energy to the very limit and also produces additional sites for OER. In this study, we have developed two different nanostructures of the 1T-$Ni_{0.2}Mo_{0.8}S_{1.8}P_{0.2}$, nanoflowers (powder, 1T-$Ni_{0.2}Mo_{0.8}S_{1.8}P_{0.2}$ NFs) for large scale synthesis and freestanding nanosheet on carbon cloth (1T-$Ni_{0.2}Mo_{0.8}S_{1.8}P_{0.2}$ NS/CC) for binder free fabrication of the electrode. Both nanostructures have large numbers of ultrathin edges, and together with active basal planes, they facilities very efficient HER and OER performance. 1T-$Ni_{0.2}Mo_{0.8}S_{1.8}P_{0.2}$ NS/CC showed HER overpotential (η_{HER}) of

55mV and OER (η_{OER}) overpotential of 286 mV at electron densities of 10 mA cm^{-2} and 40 mA cm^{-2}, respectively, whereas, 1T-$Ni_{0.2}Mo_{0.8}S_{1.8}P_{0.2}$ NFs showed η_{HER} of 99mV and η_{OER} of 305 mV at electron densities 10 mA cm^{-2} and 40 mA cm^{-2}, respectively. Finally, an overall water splitting study was carried out, the 1T-$Ni_{0.2}Mo_{0.8}S_{1.8}P_{0.2}$ NS/CC (+ -) device showed an impressively low cell potential of 1.52 V for overall water splitting and 1T-$Ni_{0.2}Mo_{0.8}S_{1.8}P_{0.2}$ NFs (+ -) devices showed a cell potential of 1.53 V, which was much lower compared to the contemporary reports. Thus, the strategy implicated in the present study could be considered as novel and proficient and would contribute significantly to the industrial scale development of highly efficient electrocatalysts based on the earth abundant materials for various energy storage and conversion applications.

Conflicts of interest

There are no conflicts to declare.

Acknowledgements

We thank Dr. Jayaraman Balamurugan, Prof. Duy Thanh Tran, Tolendra Kshetri and Huu Tuan Le for their help. We acknowledge the Basic Science Research Program (2017R1A2B3004917) of National Research Foundation (NRF), Ministry of Science and ICT, Republic of Korea for funding.

Notes and references

1 I. Dincer and C. Zamfirescu, *Sustain. Hydrog. Prod.*, 2016, **305**, 1–479.
2 M. S. Dresselhaus and I. L. Thomas, *Nature*, 2001, **414**, 332–337.
3 X. Zou and Y. Zhang, *Chem. Soc. Rev.*, 2015, **44**, 5148–5180.
4 Z. W. Seh, J. Kibsgaard, C. F. Dickens, I. Chorkendorff, J. K. Nørskov and T. F. Jaramillo, *Science,* 2017, **355**, 146.
5 S. Chu and A. Majumdar, *Nature*, 2012, **488**, 294–303.
6 H. Zhou, F. Yu, Y. Liu, J. Sun, Z. Zhu, R. He, J. Bao, W. A. Goddard, S. Chen and Z. Ren, *Energy Environ. Sci.*, 2017, **10**, 1487–1492.
7 Q. Xiong, Y. Wang, P. F. Liu, L. R. Zheng, G. Wang, H. G. Yang, P. K. Wong, H. Zhang and H. Zhao, *Adv. Mater.*, 2018, **30**, 1–7.
8 U. Gupta and C. N. R. Rao, *Nano Energy*, 2017, **41**, 49–65.
9 Q. Ding, B. Song, P. Xu and S. Jin, *Chem*, 2016, **1**, 699–726.
10 P. Liu, J. Zhu, J. Zhang, P. Xi, K. Tao, D. Gao and D. Xue, *ACS Energy Lett.*, 2017, **2**, 745–752.
11 L. Li, Z. Qin, L. Ries, S. Hong, T. Michel, J. Yang, C. Salameh, M. Bechelany, P. Miele, D. Kaplan, M. Chhowalla and D. Voiry, *ACS Nano*, 2019, **13**, 6824–6834.
12 Y. Yan, B. Xia, Z. Xu and X. Wang, *ACS Catal.*, 2014, **4**, 1693–1705.
13 K. Leng, Z. Chen, X. Zhao, W. Tang, B. Tian, C. T. Nai, W. Zhou and K. P. Loh, *ACS Nano*, 2016, **10**, 9208–9215.
14 Y. C. Lin, D. O. Dumcenco, Y. S. Huang and K. Suenaga, *Nat. Nanotechnol.*, 2014, **9**, 391–396.
15 X. Sun, J. Dai, Y. Guo, C. Wu, F. Hu, J. Zhao, X. Zeng and Y. Xie, *Nanoscale*, 2014, **6**, 8359–8367.
16 B. Shang, P. Ma, J. Fan, L. Jiao, Z. Liu, Z. Zhang, N. Chen, Z. Cheng, X. Cui and W. Zheng, *Nanoscale*, 2018, **10**, 12330–12336.
17 I. S. Kwon, T. T. Debela, I. H. Kwak, Y. C. Park, J. Seo, J. Y. Shim, S. J. Yoo, J. G. Kim, J. Park and H. S. Kang, *Small*, 2020, **16**, 2000081.
18 C. Tan, X. Cao, X. J. Wu, Q. He, J. Yang, X. Zhang, J. Chen, W. Zhao, S. Han, G. H. Nam, M. Sindoro and H. Zhang, *Chem. Rev.*, 2017, **117**, 6225–6331.
19 T. F. Jaramillo, K. P. Jørgensen, J. Bonde, J. H. Nielsen, S. Horch and I. Chorkendorff, *Science*, 2007, **317**, 100–102.
20 T. H. M. Lau, X. Lu, J. Kulhavý, S. Wu, L. Lu, T. S. Wu, R. Kato, J. S. Foord, Y. L. Soo, K. Suenaga and S. C. E. Tsang, *Chem. Sci.*, 2018, **9**, 4769–4776.
21 Q. Xiong, X. Zhang, H. Wang, G. Liu, G. Wang, H. Zhang and H. Zhao, *Chem. Commun.*, 2018, **54**, 3859–3862.
22 Z. Zheng, T. Su, J. Shi, R. Tong, H. Xiao, Q. Zhang, Y. Zhang, Z. Wang, Q. Li and X. Wang, *Nanoscale*, 2019, **11**, 22971–22979.
23 L. Bian, W. Gao, J. Sun, M. Han, F. Li, Z. Gao, L. Shu, N. Han, Z. X. Yang, A. Song, Y. Qu and J. C. Ho, *ChemCatChem*, 2018, **10**, 1571–1577.
24 X. Ren, F. Yang, R. Chen, P. Ren and Y. Wang, *New J. Chem.*, 2020, **44**, 1493–1499.
25 W. Wu, Y. Zhao, S. Li, B. He, H. Liu, X. Zeng, J. Zhang and G. Wang, *J. Colloid Interface Sci.*, 2019, **547**, 291–298.
26 L. Zhao, B. Dong, S. Li, L. Zhou, L. Lai, Z. Wang, S. Zhao, M. Han, K. Gao, M. Lu, X. Xie, B. Chen, Z. Liu, X. Wang, H. Zhang, H. Li, J. Liu, H. Zhang, X. Huang and W. Huang, *ACS Nano*, 2017, **11**, 5800–5807.
27 Y. Wang, W. Sun, X. Ling, X. Shi, L. Li, Y. Deng, C. An and X. Han, *Chem. - A Eur. J.*, 2019, 4097–4103.
28 J. Y. Xue, F. L. Li, Z. Y. Zhao, C. Li, C. Y. Ni, H. W. Gu, D. J. Young and J. P. Lang, *Inorg. Chem.*, 2019, **58**, 11202–11209.
29 C. Ray, S. C. Lee, K. V. Sankar, B. Jin, J. Lee, J. H. Park and S. C. Jun, *ACS Appl. Mater. Interfaces*, 2017, **9**, 37739–37749.
30 D. C. Nguyen, D. T. Tran, T. L. L. Doan, D. H. Kim, N. H. Kim and J. H. Lee, *Adv. Energy Mater.*, 2020, **10**, 1–14.
31 M. A. Lukowski, A. S. Daniel, F. Meng, A. Forticaux, L. Li and S. Jin, *J. Am. Chem. Soc.*, 2013, **135**, 10274–10277.
32 D. Voiry, M. Salehi, R. Silva, T. Fujita, M. Chen, T. Asefa, V. B. Shenoy, G. Eda and M. Chhowalla, *Nano Lett.*, 2013, **13**, 6222–6227.
33 S. S. Chou, N. Sai, P. Lu, E. N. Coker, S. Liu, K. Artyushkova, T. S. Luk, B. Kaehr and C. J. Brinker, *Nat. Commun.*, 2015, **6**, 1–8.
34 Q. Lu, Y. Yu, Q. Ma, B. Chen and H. Zhang, *Adv. Mater.*, 2016, **28**, 1917–1933.
35 C. G. Morales-Guio and X. Hu, *Acc. Chem. Res.*, 2014, **47**, 2671–2681.
36 J. Wang, X. Yue, Y. Yang, S. Sirisomboonchai, P. Wang, X. Ma, A. Abudula and G. Guan, *J. Alloys Compd.*, 2020, **819**, 153346.
37 T. L. Luyen Doan, D. T. Tran, D. C. Nguyen, H. Tuan Le, N. H. Kim and J. H. Lee, *Appl. Catal. B Environ.*, 2020, **261**, 118268.
38 V. H. Hoa, D. T. Tran, H. T. Le, N. H. Kim and J. H. Lee, *Appl. Catal. B Environ.*, 2019, **253**, 235–245.
39 N. Kondekar, M. G. Boebinger, M. Tian, M. H. Kirmani and M. T. McDowell, *ACS Nano*, 2019, **13**, 7117–7126.
40 U. N. Pan, V. Sharma, T. Kshetri, T. I. Singh, D. R. Paudel, N. H. Kim and J. H. Lee, *Small*, 2020, **16**, 2001691.

View Article Online
DOI: 10.1039/D0TA05865C

Graphical Abstracts/TOC:

Single-step fabrication of 1T–$Ni_{0.2}Mo_{0.8}S_{1.8}P_{0.2}$ nanoflowers and 1T–$Ni_{0.2}Mo_{0.8}S_{1.8}P_{0.2}$ freestanding nanosheet on carbon cloth with active basal planes and expanded interlayers as high performance bifunctional electrocatalysts for electrochemical water splitting.